

This work was written as part of one of the author's official duties as an Employee of the United States Government and is therefore a work of the United States Government. In accordance with 17 U.S.C. 105, no copyright protection is available for such works under U.S. Law.

Public Domain Mark 1.0

<https://creativecommons.org/publicdomain/mark/1.0/>

Access to this work was provided by the University of Maryland, Baltimore County (UMBC) ScholarWorks@UMBC digital repository on the Maryland Shared Open Access (MD-SOAR) platform.

Please provide feedback

Please support the ScholarWorks@UMBC repository by emailing scholarworks-group@umbc.edu and telling us what having access to this work means to you and why it's important to you. Thank you.

RESEARCH ARTICLE

10.1002/2016JD025483

Key Points:

- A UV-visible spectrometer, the Airborne Compact Atmospheric Mapper (ACAM), provides unprecedented high-resolution image of tropospheric NO₂
- Validation of ACAM with coincident independent ground in situ and satellite measurements suggests excellent agreement
- Geostationary satellite measurements of NO₂ could employ the retrieval algorithm and inputs implemented for ACAM

Correspondence to:

L. N. Lamsal,
lok.lamsal@nasa.gov

Citation:

Lamsal, L. N., S. J. Janz, N. A. Krotkov, K. E. Pickering, R. J. D. Spurr, M. G. Kowalewski, C. P. Loughner, J. H. Crawford, W. H. Swartz, and J. R. Herman (2017), High-resolution NO₂ observations from the Airborne Compact Atmospheric Mapper: Retrieval and validation, *J. Geophys. Res. Atmos.*, 122, 1953–1970, doi:10.1002/2016JD025483.

Received 8 JUN 2016

Accepted 23 JAN 2017

Accepted article online 25 JAN 2017

Published online 8 FEB 2017

High-resolution NO₂ observations from the Airborne Compact Atmospheric Mapper: Retrieval and validation

L. N. Lamsal^{1,2} , S. J. Janz², N. A. Krotkov² , K. E. Pickering² , R. J. D. Spurr³ , M. G. Kowalewski^{1,2}, C. P. Loughner^{2,4,5} , J. H. Crawford⁶ , W. H. Swartz⁷ , and J. R. Herman^{2,8} 
¹Goddard Earth Sciences Technology and Research, Universities Space Research Association, Columbia, Maryland, USA, ²NASA Goddard Space Flight Center, Greenbelt, Maryland, USA, ³RT Solutions, Cambridge, Massachusetts, USA, ⁴Earth System Science Interdisciplinary Center, University of Maryland, College Park, Maryland, USA, ⁵Air Resources Laboratory, NOAA, College Park, Maryland, USA, ⁶NASA Langley Research Center, Hampton, Virginia, USA, ⁷Applied Physics Laboratory, Johns Hopkins University, Laurel, Maryland, USA, ⁸Joint Center for Earth Systems Technology, University of Maryland Baltimore County, Baltimore, Maryland, USA

Abstract Nitrogen dioxide (NO₂) is a short-lived atmospheric pollutant that serves as an air quality indicator and is itself a health concern. The Airborne Compact Atmospheric Mapper (ACAM) was flown on board the NASA UC-12 aircraft during the Deriving Information on Surface Conditions from Column and Vertically Resolved Observations Relevant to Air Quality Maryland field campaign in July 2011. The instrument collected hyperspectral remote sensing measurements in the 304–910 nm range, allowing daytime observations of several tropospheric pollutants, including nitrogen dioxide (NO₂), at an unprecedented spatial resolution of 1.5 × 1.1 km². Retrievals of slant column abundance are based on the differential optical absorption spectroscopy method. For the air mass factor computations needed to convert these retrievals to vertical column abundance, we include high-resolution information for the surface reflectivity by using bidirectional reflectance distribution function data from the Moderate Resolution Imaging Spectroradiometer. We use high-resolution simulated vertical distributions of NO₂ from the Community Multiscale Air Quality and Global Modeling Initiative models to account for the temporal variation in atmospheric NO₂ to retrieve middle and lower tropospheric NO₂ columns (NO₂ below the aircraft). We compare NO₂ derived from ACAM measurements with in situ observations from NASA's P-3B research aircraft, total column observations from the ground-based Pandora spectrometers, and tropospheric column observations from the space-based Ozone Monitoring Instrument. The high-resolution ACAM measurements not only give new insights into our understanding of atmospheric composition and chemistry through observation of subsampling variability in typical satellite and model resolutions, but they also provide opportunities for testing algorithm improvements for forthcoming geostationary air quality missions.

1. Introduction

Nitrogen oxide (NO_x = NO + NO₂) emissions are regulated in many countries as nitrogen dioxide (NO₂) is associated with respiratory mortality and morbidity [Burnett et al., 2004; Samoli et al., 2006; United States Environmental Protection Agency (U.S. EPA), 2008]. NO_x contributes to the formation of surface ozone and fine particulate matter, both of which are harmful regulated pollutants. Furthermore, NO_x indirectly impacts climate through the formation of free tropospheric ozone and secondary aerosols [Shindell et al., 2009]. Major sources of NO_x include combustion, lightning, and microbial activities in soils. NO₂ is generally a short-lived air pollutant, but its lifetime varies with space and time, leading to steep gradients in concentrations with distance from sources.

Spectroscopic ground-based measurements of NO₂ started more than four decades ago [e.g., Brewer et al., 1973]. The new generation of passive remote sensing instruments is capable of providing total (e.g., Pandora) [Herman et al., 2009] and tropospheric NO₂ columns (e.g., multi-axis differential optical absorption spectroscopy) [Wittrock et al., 2004] at high temporal resolutions. The first global tropospheric NO₂ observations were made in the middle 1990s with the Global Ozone Monitoring Experiment (GOME) instrument (1995–2003) [Burrows et al., 1999]. Similar measurements, but at higher spatial resolution, have been continued with subsequent satellite instruments (e.g., Ozone Monitoring Instrument (OMI) and GOME-2) [Levelt

et al., 2006; *Callies et al.*, 2000]. Present-day low Earth orbit satellite instruments in Sun-synchronous polar orbits provide a single snapshot of global NO₂ once each day in either the late morning or the early afternoon. Very limited information on diurnal variation has been achieved by combining the data from two satellite instruments [e.g., *Boersma et al.*, 2009]. Upcoming next-generation geostationary satellite instruments [*Chance et al.*, 2013; *Juseon et al.*, 2013] will provide regional observations at fine spatial and temporal resolutions and also allow hourly tracking of emissions, transport, and chemical processing of pollution.

In dedicated campaigns and related research activities, airborne remote sensing constitutes a valuable link between ground- and space-based NO₂ observations, providing temporally and spatially resolved information [e.g., *Kowalewski and Janz*, 2009; *Merlaud et al.*, 2012; *Popp et al.*, 2012; *Walter et al.*, 2012; *Oetjen et al.*, 2013; *Liu et al.*, 2015; *Nowlan et al.*, 2016]. Airborne measurements can also serve as a test bed for both instrument design and retrieval algorithm development for future geostationary satellite instruments [e.g., *Nowlan et al.*, 2016]. Retrieval algorithms that have been developed and tested for previous and current satellite instruments do not necessarily apply for geostationary observations taken over the entire day. Certain input parameters, such as the vertical distribution of NO₂, required by the retrieval algorithm, vary diurnally, potentially introducing diurnally varying systematic errors in retrievals from geostationary satellites. Campaign-based airborne retrieval algorithm development can take advantage of valuable measurements of many retrieval parameters that, in turn, can refine geostationary algorithms. Moreover, with their improved sensitivity to boundary layer NO₂ and the ability to cover the spatial extent of satellite pixels, airborne instruments can produce credible and independent measurements for the assessment and validation of satellite retrievals.

This paper presents the first in-depth retrieval study for NO₂ from the Airborne Compact Atmospheric Mapper (ACAM), an ultraviolet (UV)/visible/near-infrared spectrometer that flew on board the NASA UC-12 aircraft during the Deriving Information on Surface Conditions from Column and Vertically Resolved Observations Relevant to Air Quality (DISCOVER-AQ) field campaign in Maryland in July 2011. An earlier study by *Liu et al.* [2015] was focused on characterization of ACAM radiance measurements and testing of slant column retrievals. Our main objectives are (i) to design and describe a retrieval scheme to derive vertical NO₂ column abundance underneath the aircraft from the airborne spectrometer and (ii) to provide a quantitative assessment of the resulting NO₂ product. This approach will be applied to other similar measurements made at other DISCOVER-AQ locations. Section 2 describes the ACAM measurements and various concurrent data sources used in this study. We present the retrieval algorithm in section 3. Comparisons of ACAM retrievals with results from other instruments are presented in section 3.4. Section 4 has concluding remarks.

2. NO₂ Observations and Models

2.1. DISCOVER-AQ Field Campaign

One of the objectives of the NASA Earth Venture 1 DISCOVER-AQ (Deriving Information on Surface Conditions from Column and Vertically Resolved Observations Relevant to Air Quality; <http://www-air.larc.nasa.gov/missions/discover-aq/discover-aq.html>) field program is to provide vertically resolved measurements that will help improve the application of satellite observations to diagnose surface air quality. This paper focuses on the first of four DISCOVER-AQ field deployments, that is, the campaign conducted in the Baltimore-Washington D.C. metropolitan region in July 2011. As part of this campaign, a large suite of NO₂ observations was made, including NO₂ columns from the nadir-viewing ACAM spectrometer on board the NASA UC-12 aircraft, in situ NO₂ concentrations from the chemiluminescence monitor on board the NASA P-3B aircraft, NO₂ columns from the ground-based Pandora spectrometer at 12 air-quality monitoring sites, and surface NO₂ concentrations from commercial and research grade chemiluminescence NO_x monitors. Retrospective modeling for the campaign period was performed with the Weather Research and Forecasting Community Multiscale Air Quality (WRF-CMAQ) model. In this work, we use in situ and Pandora NO₂ measurements to evaluate both CMAQ-simulated NO₂ profiles and ACAM retrievals.

2.1.1. ACAM Observations

The NASA UC-12 aircraft has been the primary platform for the ACAM spectrometers [*Kowalewski and Janz*, 2009]. The instrument package can be operated autonomously to collect hyperspectral measurements in the UV, visible, and near-infrared range (304–910 nm). ACAM consists of two thermally stabilized miniature spectrometers, one covering the spectral range from 304 nm to 520 nm with a resolution of

0.8 nm and a sampling of 0.105 nm, and another covering 460 nm to 900 nm with a resolution of 1.7 nm and a sampling of 0.21 nm. The former is referred to as the Air Quality Spectrometer, which provides remote sensing observations of tropospheric pollutants including NO₂. A description of the spectral performance testing can be found in Kowalewski and Janz [2009]. During the DISCOVER-AQ Maryland campaign, 26 flights were made, flying ~4 h sorties usually twice each day. The ACAM nadir viewing geometry is defined by a scan mirror that moves in ten discrete equivalent sized steps from port to starboard, orthogonal to the aircraft track. The full mirror scan range defines a $\pm 23^\circ$ field-of-regard across-track in the nadir direction. The flight altitude of the UC-12 aircraft was typically 8 km at a nominal ground speed of 100 m/s. This combination of instrument scan range, aircraft altitude, and speed resulted in an ACAM native ground resolution of 0.5 km \times 0.75 km per ground pixel. In order to improve the signal-to-noise ratio of the measurements, we applied a pair-average coadding scheme to generate NO₂ observations at a resolution of ~1.5 km (cross track) \times 1.1 km (along track). A high-definition video camera mounted inside ACAM allows for visual detection of clouds. Since its first deployment during the Aura Validation Experiment 2 in June 2005, the ACAM instrument has participated in several flight campaigns and was upgraded with various technological advancements, such as a zenith viewing fiber and higher sensitivity spectrometers, to improve its sensitivity to trace-gas absorption.

2.1.2. In Situ Aircraft Measurements

The NASA P-3B aircraft measured the vertical distribution of NO₂ by profiling over six surface air-quality monitoring sites. In situ NO₂ observations from the aircraft offer a unique opportunity to evaluate simulated a priori NO₂ profiles and ACAM NO₂ column retrievals. The P-3B aircraft made measurements during the day (between 7 A.M. and 7 P.M.) with typically three vertical spirals per day over each surface site. In the course of 14 flight days, each location had a total of 38 to 45 spirals of ~4 km radius with numerous 1 s observations, covering altitudes from 300 m up to 5 km. The time to accomplish one complete spiral was ~20 min. NO₂ measurements were carried out with (1) the thermal dissociation laser-induced fluorescence (TD-LIF) instrument [Thornton *et al.*, 2000; Day *et al.*, 2002] from the University of California, Berkeley, and (2) the four-channel chemiluminescence instrument (P-CL) from the National Center for Atmospheric Research [Ridley and Grahek, 1990; Ridley *et al.*, 2004]. The TD-LIF instrument took alternating measurements of various reactive nitrogen species, with the result that the low NO₂ sampling frequency was insufficient to resolve the sharp vertical gradient in the boundary layer. Therefore, in this study, we only use NO₂ measurements from the P-CL instrument, with an uncertainty <10% and a 1 s, 2σ detection limit of 50 parts per thousand by volume.

2.1.3. Pandora Observations

Ground-based Pandora spectrometers [Herman *et al.*, 2009] provided total NO₂ column measurements by direct Sun observations at a sampling period of 90 s. Pandora is a small commercially available moderate-resolution (0.5 nm) UV/visible (280–525 nm) spectrometer system capable of providing observations of various trace gases. Pandora NO₂ retrievals are based on the differential optical absorption spectroscopy (DOAS) technique, with total NO₂ column data with a temporal resolution of 90 s, a precision of $\sim 2.7 \times 10^{14}$ molecules cm⁻², and an accuracy of $\sim 2.7 \times 10^{15}$ molecules cm⁻².

2.2. Simulation of NO₂ and Aerosol

Orbital and suborbital NO₂ retrievals rely on the simulated vertical distribution of NO₂ as an input. Since retrieval errors arising from a priori NO₂ profiles can be quite large [e.g., Hains *et al.*, 2010; Heckel *et al.*, 2011; Russell *et al.*, 2011; Lamsal *et al.*, 2014], it is critically important to have realistic information on the vertical distribution of NO₂ throughout the atmospheric column. While some well-tested global models can offer vertical NO₂ profiles for the entire atmosphere and may perform reasonably well in both the free-troposphere and stratosphere due to the relatively smooth NO₂ field there, their coarse spatial resolution hinders them from capturing the spatial variability of NO₂ in the planetary boundary layer (PBL). In contrast, regional models are generally tropospheric only but may offer a more accurate representation of NO₂ within the PBL due to the use of high spatially resolved emissions and chemical and physical processes. In this work, we combine information on a priori NO₂ profiles from global and regional models, taking advantage of their relative strengths to improve the retrievals and reduce retrieval errors.

NO₂ vertical profiles exhibit diurnal variation due to diurnal changes in several factors including emissions, mixing layer depth, and the photochemically driven partitioning of nitrogen oxide species. The latter is a dominating process in the stratosphere, manifesting as a monotonic increase in NO₂ during daylight

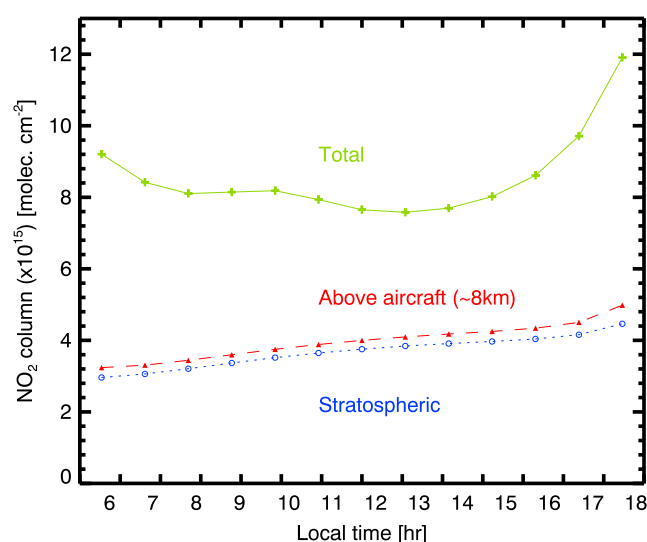


Figure 1. Hourly variation in GMI-simulated total (green), stratospheric (blue), and above aircraft (red) NO₂ column over the DISCOVER-AQ domain (37–40°N, 74–79°W) on 1 July 2011.

Chem model [Bey *et al.*, 2001] and is driven by GEOS 5 meteorological fields [Rienecker *et al.*, 2008] at a resolution of 2° latitude × 2.5° longitude. The model extends vertically from the surface to 0.01 hPa, with 72 levels and a vertical resolution ranging from ~150 m in the boundary layer to ~1 km in the free troposphere and lower stratosphere. We sample hourly model profiles for use in our retrievals and for a self-consistent comparison with observational data sets.

Figure 1 shows daytime changes in total and stratospheric columns and column above the typical altitude of ACAM measurements over the DISCOVER-AQ domain on 1 July 2011. In the stratosphere, NO₂ exhibits significant diurnal variation, with monotonic increase in NO₂ column from ~3.0 × 10¹⁵ molecules cm⁻² at 6 A.M. to ~4.5 × 10¹⁵ molecules cm⁻² at 6 P.M., an increase of 50%. The GMI-simulated diurnal variation of stratospheric NO₂ has been previously evaluated with ground-based multi-function DOAS measurements and reported to agree within 6% [Spinei *et al.*, 2014]. The observed diurnal variation of tropospheric NO₂ is the result of diurnal changes in NO_x emissions, PBL mixing, and chemistry. GMI simulates the free-tropospheric NO₂ fairly well [Lamsal *et al.*, 2014].

2.2.2. High-Resolution CMAQ Simulation

We used the Environmental Protection Agency's Community Multiscale Air Quality (CMAQ) [Byun and Schere, 2006] model version 5.0 to simulate NO₂ with a horizontal resolution of 4 km and 45 vertical levels from the surface to 100 hPa. At this horizontal resolution, CMAQ is capable of simulating local scale bay breeze circulations [Loughner *et al.*, 2011]. An enhanced vertical resolution with 16 levels covering the lowest 2 km allows accurate simulation of boundary layer processes. The model was driven by a meteorological field from the Weather Research and Forecasting (WRF version 3.3) [Skamarock *et al.*, 2008] model. The WRF simulation included the mesoscale model version 5 similarity surface layer scheme [Zhang and Anthes, 1982], the National Centers for Environmental Prediction Oregon State University, the Air Force and Hydrologic Research Laboratory Land Surface Model [Tewari *et al.*, 2004], and the Yonsei University PBL scheme [Hong and Lim, 2006].

The CMAQ simulation was based on (1) the Carbon Bond 05 gas-phase chemical mechanism [Yarwood *et al.*, 2005], (2) CMAQ's fifth-generation modal aerosol model, (3) Asymmetric Convective Model (ACM) version 2 for calculating vertical diffusion, (4) ACM [Pleim and Chang, 1992] to compute convective mixing and containing the heterogeneous chemistry scheme in CMAQ, and (5) a new dry deposition module (known as M3Dry) for calculating dry deposition [Pleim *et al.*, 2001]. Emissions were as described in Loughner *et al.* [2014], with mobile emissions reduced by 50% as discussed in Anderson *et al.* [2014]. The photolysis frequency of alkyl nitrate was increased by a factor of 10 [Anderson *et al.*, 2014]. Chemical initial and boundary conditions came from a 12 km CMAQ simulation covering the continental U.S. We conducted a simulation for July 2011 and sampled the model hourly for analysis of the ACAM data.

hours. Chemical models with a detailed stratospheric chemical mechanism have been shown to capture the diurnal variation accurately [e.g., Bracher *et al.*, 2005].

2.2.1. GMI Simulation

We use the Global Modeling Initiative (GMI) chemical transport model [Strahan *et al.*, 2007] to simulate NO₂ amounts. The model simulates the stratosphere and troposphere and includes emissions, aerosol microphysics, chemistry, deposition, radiation, advection, and other important chemical and physical processes. Emissions are similar to those used in the standard simulation, as discussed in Strode *et al.* [2015]. The GMI chemical mechanism combines the stratospheric mechanism described by Douglass *et al.* [2004] with a detailed tropospheric O₃-NO_x-hydrocarbon chemistry originating from the Harvard GEOS-

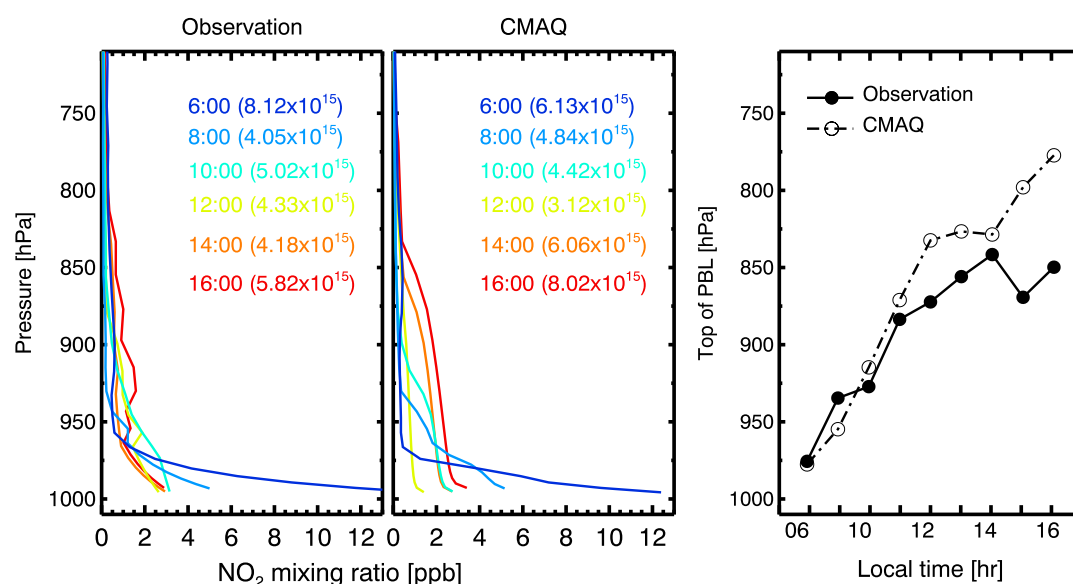


Figure 2. Vertical distribution of NO_2 and top of PBL pressure over Padonia, MD, during DISCOVER-AQ. The colored lines show the average hourly NO_2 profiles derived from the (left) in situ measurements and (middle) CMAQ simulation at different local times. The column amounts below 700 hPa, expressed in molecules cm^{-2} unit, are given in the legend. (right) The diurnal variation in observed (solid line) and simulated (dashed line) PBL top pressures.

Here we compare hourly mean vertical NO_2 profiles calculated by CMAQ with surface and aircraft measurements during the DISCOVER-AQ field campaign. Figure 2 compares average NO_2 profiles over Padonia, Maryland, from in situ measurements with those calculated with the CMAQ model. The model results are broadly consistent with the measurements with a minimum in the early afternoon. The profile of NO_2 shows a maximum concentration at the surface, decreases rapidly near the top of mixing layer, and exhibits gradual change with the mixing layer depth. Differences are observed in the vertical gradient, suggesting that there are some concerns with emission levels, and perhaps also with overly rapid mixing within the PBL in the model. Modeled concentrations are more than a factor of 3 lower than the measurements in the free troposphere (above 800 hPa).

2.2.3. GEOS-Chem Simulation

To account for the effect of aerosols in the air mass factor (AMF) calculations, we require type-specific vertical profiles of the aerosol extinction coefficient, single-scattering albedo, and scattering matrices. We rely on a model for the first two of these quantities. Since these fields were not archived by either the GMI or CMAQ models, they are taken from the nested GEOS-Chem three-dimensional model of tropospheric chemistry [Bey et al., 2001] at 2° longitude \times 1° latitude with 47 vertical layers (version 9-01-03) [van Donkelaar et al., 2014; Lamsal et al., 2014]. The GEOS-Chem and GMI models share similar tropospheric O_3 - NO_x -hydrocarbon chemical mechanisms, meteorological data, and emissions [Lamsal et al., 2014; Strode et al., 2015], making these two models generally consistent. Details on emissions and boundary conditions for our GEOS-Chem nested simulations over North America (10° – 70° N, 40° – 140° W) can be found in Lamsal et al. [2014]. For aerosols, the GEOS-Chem model simulates sulfate, nitrate, ammonium, black and organic carbon, dust, and sea salt [Park et al., 2006; Fairlie et al., 2010; Jaeglé et al., 2011]. Simulation of sulfate, nitrate, and ammonium aerosols follows the thermodynamical equilibrium scheme as described in Fountoukis and Nenes [2007]. Fluxes of mineral dust are calculated by using the dust entrainment and deposition mobilization scheme [Zender et al., 2003]. Aerosol microphysical properties are characterized by dry size distributions, hygroscopic growth factors, and refractive indices and follow Drury et al. [2010].

2.3. OMI Observations

The OMI offers early afternoon (local time 1300–1430) NO_2 column abundances at a spatial resolution of $13 \times 24 \text{ km}^2$ at nadir and $\sim 30 \times 160 \text{ km}^2$ at swath edges with daily global coverage. We use the tropospheric NO_2 column data as described in Bucsela et al. [2013] and Lamsal et al. [2014] but with improved slant

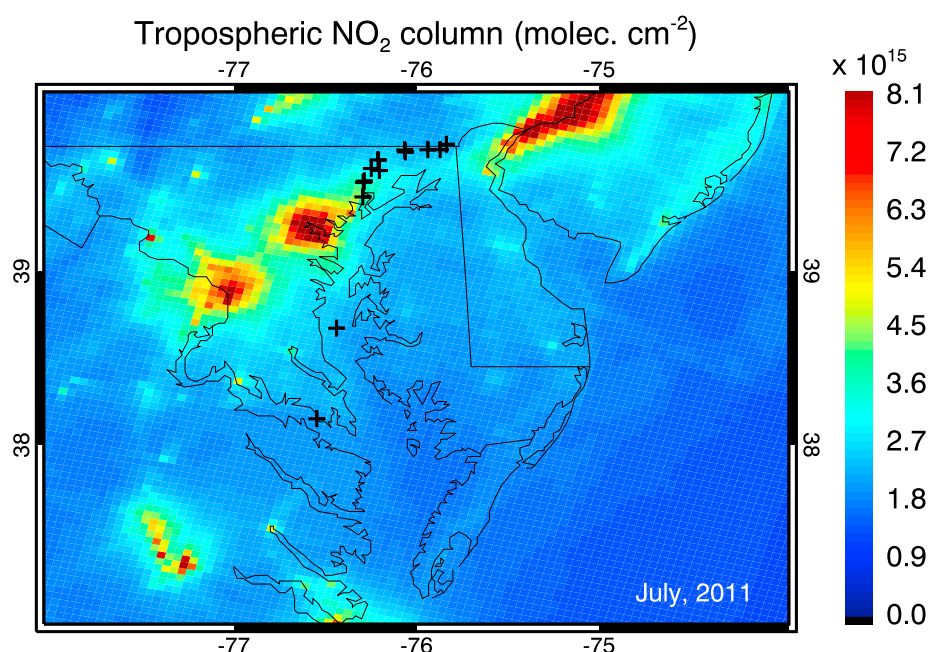


Figure 3. Early afternoon (1–2 P.M.) monthly mean CMAQ tropospheric NO₂ column at 4 km × 4 km for July 2011 over the DISCOVER-AQ domain. The symbols show the location of reference measurements used for ACAM NO₂ retrievals.

column retrievals as described in *Marchenko et al.* [2015] and high-resolution NO₂ profiles for more accurate AMF calculation as discussed in *Lamsal et al.* [2015]. The estimated errors in the tropospheric NO₂ columns over polluted regions ($>10^{15}$ molecules cm⁻²) under clear-sky conditions (cloud radiance fraction <0.5) are estimated to be $<30\%$ [Bucsela et al., 2013]. Here we compare individual clear-sky OMI and ACAM observations coincident in space and time (within ± 10 min). We exclude OMI pixels affected by the so-called row anomaly [Dobber et al., 2008], but we do use data from all scan positions where available.

3. ACAM NO₂ Retrievals and Evaluation

In this section, we discuss our approach to derive the NO₂ vertical column density (VCD) below the aircraft and then focus on the evaluation of the product. The retrieval approach is similar to that applied to satellite NO₂ retrievals, but it requires some modifications due to the much lower measurement altitude and the lack of top-of-atmosphere irradiance measurements.

3.1. Differential NO₂ SCD

To obtain slant column densities (SCDs) from ACAM-measured reflectance spectra, we use the well-known differential optical absorption spectroscopy (DOAS) fitting method [Platt and Stutz, 2006]. ACAM cannot provide solar irradiance reference spectra as is usually required by the DOAS fitting, so instead we use an average daily earthshine spectrum derived from ~ 400 consecutive earthshine spectra measured over 6 min intervals over an unpolluted background location (Figure 3). This averaging approach improves the signal-to-noise ratio of the reference spectrum and minimizes errors in the retrievals. The reference location had to be changed daily to avoid any local NO₂ enhancements. The fitting algorithm QDOAS (<http://uv-vis.aeronomie.be/software/QDOAS/>) used here is a robust, flexible, and well-validated open source software that has been used to perform DOAS retrievals of trace gases from satellite [e.g., Anand et al., 2015] and aircraft-based [e.g., Merlaud et al., 2012] measurements. The spectral fitting is performed in the range of 425–460 nm. The QDOAS algorithm fits the reference and a series of convolved laboratory-measured trace gas absorption spectra simultaneously in order to perform the wavelength calibration. Fitted trace gases and parameters include NO₂ [Vandaele et al., 1998], O₃ [Bass and Paur, 1985], H₂O [Rothman et al., 2005], CHOCHO [Volkamer et al., 2005], O₂-O₂ [Greenblatt et al., 1990], reference Ring spectrum [Chance and Spurr, 1997],

and a third-order polynomial function in wavelength. The closure polynomial models the slowly varying spectral signatures due to aerosols and molecular absorption and scattering, instrumental features, and reflection at the Earth's surface. The temperature dependence of the NO₂ cross section is accounted for in the calculation of the air mass factor (AMF) (next section). With our average earthshine spectra, the DOAS spectral fit for each ACAM pixel will yield the differential (rather than absolute) NO₂ SCD, that is, with respect to the SCD at the reference location.

3.2. Calculation of NO₂ AMF by Using Vector Linearized Discrete Ordinate Radiative Transfer Code

Retrieved NO₂ SCDs are converted to VCDs with division by AMFs, which we compute by using the vector linearized discrete ordinate radiative transfer code (VLIDORT) [Spurr, 2008]. VLIDORT is a multiple-scattering model that calculates radiances and weighting functions simultaneously in a multilayer atmosphere. Weighting functions (Jacobians) are the fields of analytic radiance derivatives with respect to atmospheric and surface variables. VLIDORT has an exact treatment for the single scattering, treating the solar and line-of-sight attenuation in a curved atmosphere, and it uses the pseudospherical approximation (solar attenuation in a curved atmosphere) for the multiple-scattering computation. Simulations from the VLIDORT model have been validated against benchmark results from other models [Spurr, 2008, and references therein].

The NO₂ AMFs are highly sensitive to surface reflectivity and the vertical distribution of NO₂ and aerosols. The bidirectional reflectance distribution function (BRDF) model describes the distribution of reflected light at a surface and exhibits dependence on the wavelength and incoming and outgoing light directions. In contrast to the Lambertian (isotropic reflectance) assumption that is commonly used in satellite trace gas retrievals, the BRDF addresses directional reflectance effects that are present in orbital and suborbital remote sensing observations. In addition to the Lambertian surface, VLIDORT has a supplement which calculates BRDFs for a number of surface models.

Here we calculate AMFs, first with the Lambertian surface assumption to illustrate the importance of surface reflectivity in the ACAM NO₂ retrievals, and second using non-Lambertian surface BRDFs for the actual retrievals. For the latter, we select the RossThick and LiSparse kernel functions that are used in the Moderate Resolution Imaging Spectroradiometer (MODIS) BRDF model; these kernels are included in the VLIDORT supplement. The MODIS Channel 3 (459–479 nm) gap-filled BRDF Collection 5 product [Schaaf *et al.*, 2011] used here is composed of three kernel coefficients (isotropic, volumetric, and geometric) which characterize the complete surface BRDF. The coefficients are available at a spatial resolution of 30 arc sec and a temporal resolution of 8 days (derived from clear-sky data over a 16 day interval). The MODIS product is also available over coastal areas and inland waters, albeit with reduced accuracy. The channel 3 data are closest in wavelength to the value used in our AMF calculations (440 nm, close to the center of the NO₂ spectral fitting window). For optically thin absorbers such as NO₂, the mean optical path of scattered photons is nearly independent of wavelength within the NO₂ fitting window.

VLIDORT requires optical property inputs appropriate to scattering and absorption by air molecules and aerosols. To account for the effect of aerosols in the AMF calculations, we use July average type-specific vertical profiles of aerosol extinction coefficient, aerosol optical depth (AOD), and single-scattering albedo computed with the nested GEOS-Chem simulation discussed in section 2.2.3. The model AODs were constrained by daily observations from MODIS. The scattering matrices and their expansion coefficients (in terms of the generalized spherical functions used by VLIDORT) are computed with a linearized Mie code [Spurr *et al.*, 2012].

As discussed in the next section (section 3.2.1), ACAM measurements have significant NO₂ sensitivity above the aircraft. Our GMI simulated results suggest that the NO₂ column above the aircraft is only ~8% higher than the stratospheric NO₂ column. Despite the low concentration, it is important to account for NO₂ above the aircraft. An evaluation of GMI simulations with in situ measurements suggests that GMI simulates free tropospheric NO₂ reasonably well, although the model may not be able to capture day-to-day variability in the lightning NO_x emissions [Lamsal *et al.*, 2014; Flynn *et al.*, 2016]. Since the CMAQ-simulated NO₂ concentrations are considerably lower than the measurements in the free troposphere, we improve the knowledge of the vertical distribution of NO₂ by combining information from the two models. Here our a priori vertical profiles of NO₂ are constructed as hourly monthly averages from the CMAQ model output in the PBL and from the GMI model elsewhere in the atmosphere. The model profiles are merged within two model layers above the top of the PBL in order to generate smoothly varying profiles with height.

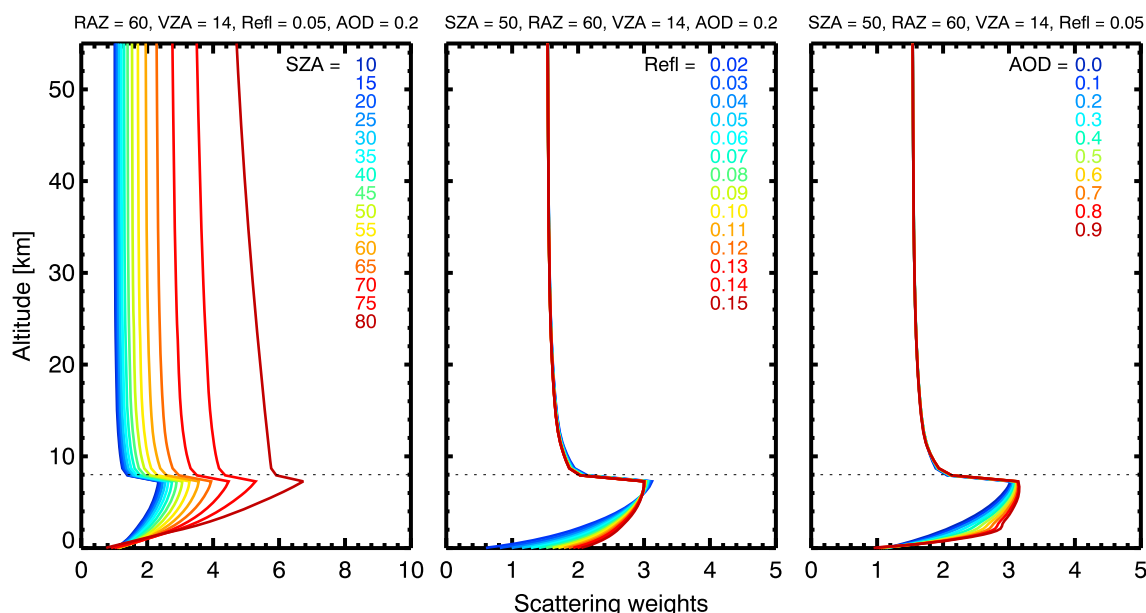


Figure 4. Vertical distribution of scattering weights for various values of (left) solar zenith angle (SZA), (middle) surface reflectivity (Refl), and (right) aerosol optical depth (AOD). Other quantities, such as relative azimuth angle (RAZ) and viewing zenith angle (VZA), are kept constant as indicated. The horizontal dotted line indicates the aircraft altitude.

3.2.1. Vertically Resolved NO₂ Sensitivity

We calculate altitude-dependent scattering weights (w) for ACAM measurement conditions by using VLIDORT. Scattering weights, which are identical to box-AMFs for optically thin absorbers, describe the sensitivity of the measurements as a function of altitude. They are calculated as the logarithmic intensity partial derivative with respect to the vertical NO₂ absorption optical thickness for each model layer [Palmer *et al.*, 2001]. Figure 4 shows how scattering weights vary with altitude for ACAM's typical measurement conditions at a flight altitude of 8 km. ACAM's NO₂ sensitivity is highest at and below the layer where the aircraft is located, but there is also considerable sensitivity above the aircraft, which changes rapidly with solar zenith angle. Below the aircraft, the sensitivity decreases gradually toward the surface. Below-aircraft sensitivity is enhanced over bright surfaces and in the presence of nonabsorbing aerosols that are dominant over the eastern U.S. in summer.

3.2.2. AMF Sensitivity to Parameters

To account for the effect of changes in sensitivity due to variations in observational geometry and atmospheric and surface properties over the course of the day, we compute AMFs underneath and above the aircraft by integrating the product of vertical distribution of scattering weights and the a priori NO₂ profile:

$$\text{AMF}_{\downarrow} = \frac{\sum_{\text{surface}}^H w \times x_a}{\sum_{\text{surface}}^H x_a}$$

$$\text{AMF}_{\uparrow} = \frac{\sum_H^{\text{TOA}} w \times x_a}{\sum_H^{\text{TOA}} x_a},$$

where x_a represents the partial layer NO₂ column. The summation extending from the surface to aircraft altitude (H) gives the AMF underneath the aircraft (AMF_{\downarrow}), and that extending from H to the top of the atmosphere (TOA) provides the AMF above the aircraft (AMF_{\uparrow}).

We conduct a series of sensitivity simulations for typical ACAM observational geometry and typical atmospheric and surface properties (NO₂, aerosol, temperature profiles, and surface reflectivity) over the DISCOVER-AQ domain. Figure 5 shows how AMF_{\downarrow} and AMF_{\uparrow} vary with surface reflectivity, aerosol amount, and solar and viewing angles for a typical flight altitude of 8 km. The AMF_{\uparrow} is not equal to the geometric AMF (AMF_{geo}) calculated as a function of solar (SZA) and viewing zenith angles (VZA) (i.e., $\text{AMF}_{\text{geo}} = \sec(\text{SZA}) + \sec(\text{VZA})$), but the two AMFs do vary strongly with SZA and are highly correlated.

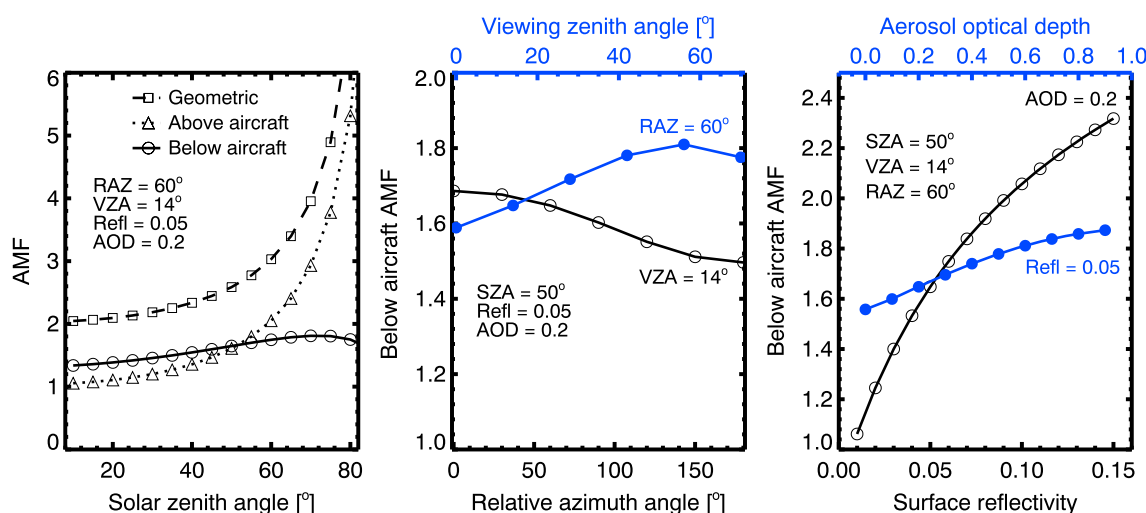


Figure 5. AMF dependencies for various inputs. (left) AMFs underneath (solid line with open circles) and above (dotted line with triangles) the aircraft are compared with geometric AMF (dashed line with squares) for various SZAs. (middle) AMF below aircraft versus RAZ at VZA of 14° (black) and AMF below aircraft versus VZA at RAZ of 60° (blue). (right) AMF below aircraft versus surface reflectivity at AOD of 0.2 (black) and AMF below aircraft versus AOD at reflectivity of 0.05 (blue). Other values that are kept constant as indicated.

Changes in AMF_{\downarrow} with observational angles and AOD are rather small, usually $<15\%$ for VZA and relative azimuth angle (RAZ), $<35\%$ for SZA, and $<20\%$ for AOD. The AMF_{\downarrow} is highly sensitive to surface reflectivity by more than a factor of 2 (Figure 5, right).

3.2.3. Relationship Between Actual and Geometric AMFs

Previous studies on NO_2 vertical column retrievals from airborne spectrometers have relied on either geometric [e.g., Oetjen *et al.*, 2013] or full radiative transfer (RT) AMF calculations [Merlaud *et al.*, 2012; Popp *et al.*, 2012; Nowlan *et al.*, 2016]. Here we explore how geometric AMFs relate to full RT AMFs and how their relationship changes with different observational, surface, and aerosol conditions. Our aim here is to conduct an independent analysis by using VLIDORT and extend the work of Baidar *et al.* [2013], who discussed an application of a simple geometric approximation to convert SCDs of trace gas measurements from the University of Colorado Airborne MAX-DOAS instrument to VCDs during the California Research at the Nexus of Air Quality and Climate Change field campaign. This instrument was deployed on board the NOAA Twin Otter remote sensing research aircraft, taking measurements at altitudes <4 km and SZAs $<60^\circ$.

Figure 6 compares full RT AMFs (AMF_{\downarrow}) with geometric AMFs under various observational, surface, and aerosol conditions. Like AMF_{geo} , AMF_{\downarrow} not only increases with SZA but also decreases with flight altitude. For small SZA, the AMF_{\downarrow} for aircraft located at about 4 km altitude is larger than that for satellite by about a factor of 2 [Oetjen *et al.*, 2013]. As the sensor altitude lowers, Rayleigh-scattered photons diminish and the contribution of photons reflected from the surface and scattered on particles in the PBL increases. These Rayleigh-scattered photons contain little information about NO_2 in the boundary layer, making AMF_{\downarrow} closer to the geometrical value. Therefore, AMF_{\downarrow} can be approximated by AMF_{geo} , but only for certain conditions defined by values of view angles, flight altitude, surface reflectivity, and the amount and distribution of aerosols. For instance, the geometric approximation works well for flight altitude in the range of 2–4 km, if SZA $<50^\circ$. Figure 6 shows various reflectivity- and aerosol-specific aircraft trajectories (altitude) necessary for the geometric approximation. To apply such approximation, the aircraft must fly closer to the ground (<2 km altitude) if measurements are performed in the clean atmosphere and over dark surfaces. Due to increases in vertical sensitivity over bright surfaces and in the presence of scattering aerosols, the flight altitude needs to be higher to maintain the geometric approximation.

Our sensitivity study suggests that the geometric AMF approximation is generally not applicable to ACAM because of the higher flight altitudes. However, the study has practical implications for future aircraft campaigns. With prior knowledge of the underlying surface conditions and concurrent aerosol measurements, it is possible to develop flight strategies that would allow the retrieval approach to use the geometric

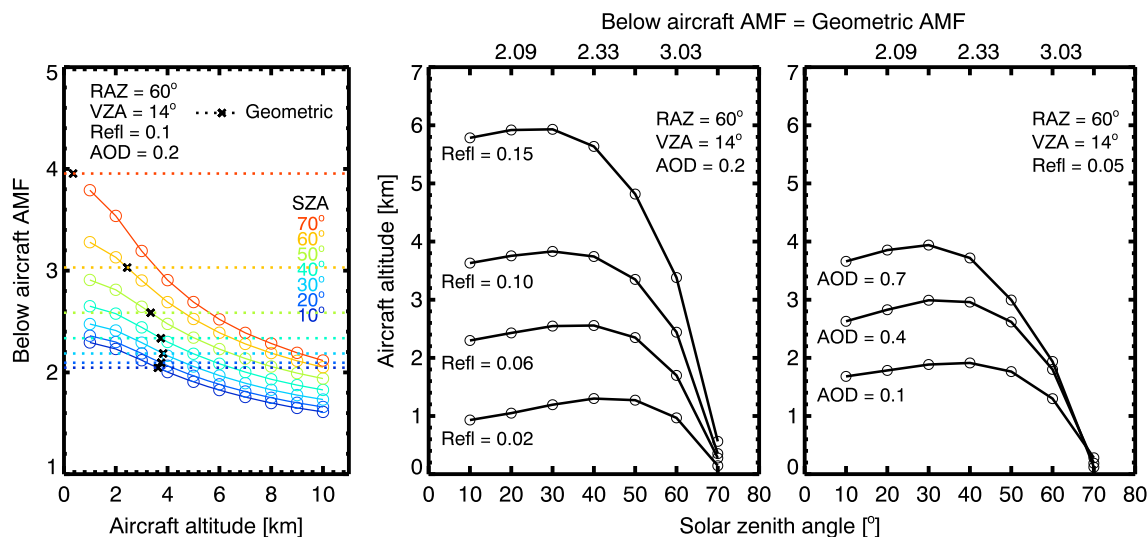


Figure 6. Relationship between geometric and below aircraft AMFs. (left) Changes in below aircraft AMF with aircraft altitudes for various SZAs (colored lines) are compared with geometric AMF (horizontal dotted lines). Actual AMF is equal to geometric AMF at the intersection of the two lines (plus symbols). (middle) Aircraft altitudes at which actual AMFs are equal to geometric AMFs, plotted as a function of SZAs and surface reflectivities. (right) Aircraft altitudes at which actual AMFs are equal to geometric AMFs, this time varying with SZAs and AODs. Other values are kept constant as indicated.

approximation. Application of AMF_{geo} to convert slant to vertical column not only simplifies the retrieval approach considerably, but it could also enhance data quality, since the AMF conversion will then be independent of some of the model parameter inputs that are not known with much certainty (e.g., NO_2 vertical profiles).

3.3. Calculation of NO_2 VCD Below Aircraft

The differential SCD ($d\Omega_s$) obtained from the DOAS fit discussed in section 3.1 represents the difference in SCD between measured and reference spectra:

$$d\Omega_s = \Omega_s - \Omega_s^R,$$

where Ω_s and Ω_s^R represent slant columns at target and reference locations, respectively. The separation of the total SCD into two components (above and below the aircraft) and conversion into the respective VCDs yield:

$$\Omega_v \downarrow = \frac{d\Omega_s - \Omega_v \uparrow \times A \uparrow + (\Omega_v^R \downarrow \times A^R \downarrow + \Omega_v^R \uparrow \times A^R \uparrow)}{A \downarrow}.$$

Here Ω_v and Ω_v^R are VCDs and A and A^R are AMFs at target and reference locations, respectively. The arrows denote quantities above (\uparrow) or beneath (\downarrow) the aircraft. VCDs at the reference location are simulated NO_2 columns temporally adjusted to match colocated OMI retrievals. As noted already, model NO_2 profiles are derived from coincidently sampled NO_2 profiles from CMAQ and GMI by merging them around the top of PBL. Spatial averaging for VCDs and AMFs is consistent with that for reference spectra. Elsewhere, VCDs above the aircraft are the integral of coincidently sampled GMI NO_2 profiles adjusted to coincidently sampled OMI stratospheric NO_2 columns. Therefore, our calculation of NO_2 VCD below the aircraft accounts for both spatial and temporal variations of NO_2 above the aircraft.

Figure 7 shows examples of ACAM NO_2 VCDs below the aircraft observed on 29 July 2011. The flight path was repeated typically three times each day, providing high temporally resolved NO_2 observations over the course of the day. The spatial pattern in NO_2 reflects the distribution of NO_x sources with enhancements over cities, industrial areas, and highways. The observed diurnal pattern is consistent with that observed by surface monitors [e.g., Lamsal et al., 2008]. Daytime photochemical loss and reduced vehicular emissions result in low NO_2 columns in the late morning/early afternoon. Enhancement in the late afternoon is due, in part, not only to increases in traffic volume typical of the Washington-Baltimore corridor but also to declines in the photolysis rates and the shrinking of the mixed layer depth [e.g., Poulida et al., 1994].

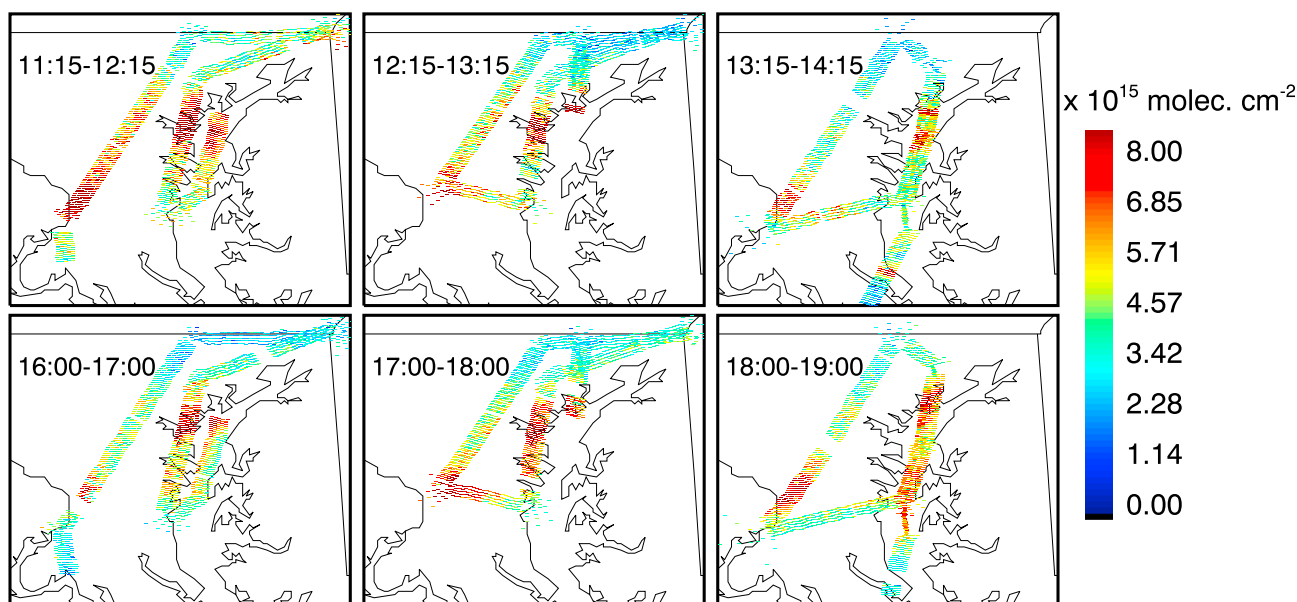


Figure 7. ACAM NO₂ VCD (below aircraft) observations for six flight patterns on 29 July 2011 during the Maryland-Washington DISCOVER-AQ field campaign. The repeated flight patterns allow observation of diurnal changes in NO₂.

3.4. Uncertainty in ACAM NO₂ Retrievals

The overall error budget of NO₂ VCDs below the aircraft is composed of errors in differential NO₂ SCDs and AMFs. The estimated uncertainty in the differential SCD is 1.1×10^{15} molecules cm⁻². The AMF errors arise from uncertainty in a priori NO₂ profile shapes and in the parameters that affect the scattering weights as discussed in section 3.2.2. Since our interest is cloud-free ACAM observations, we neglect the uncertainties arising from cloud parameters (cloud pressure and cloud radiance fraction) that can also affect scattering weights. The AMF uncertainty from the ACAM viewing geometry is negligible. Our analysis shows that the overall error in individual NO₂ VCD below aircraft, derived through propagation of errors, is estimated to be 31%.

The errors in the a priori profiles can introduce both random (due to differences between daily and monthly mean profiles) and systematic (due to model deficiencies in capturing observed spatial and temporal variabilities) errors. To quantify these errors, respectively, we performed retrievals by using (1) modeled day-specific and monthly average NO₂ profiles and (2) modeled and P-3B observed NO₂ profiles as a priori. Replacing day-specific NO₂ profiles by monthly average profiles suggested 10% uncertainty in ACAM NO₂ VCDs, although the two retrievals at times differed by as much as 50%, as previously reported [Hains et al., 2010; Heckel et al., 2011; Russell et al., 2011; Valin et al., 2011; Lamsal et al., 2014; Laughner et al., 2016]. Our analysis of AMFs calculated with modeled and measured monthly average NO₂ profiles at a site in Padonia, Maryland, suggests diurnally varying retrieval errors, reaching up to 15% for certain times of day. This error is model dependent and can be much larger for less accurate models.

Surface reflectivity is one of the largest contributors to AMF uncertainty [Martin et al., 2002; Zhou et al., 2010; Vasilkov et al., 2016]. Our accounting for surface reflectance anisotropy with MODIS high-resolution BRDF data reduces this error considerably. Assuming similar uncertainty in the MODIS BRDF data and surface reflectivity (the MODIS theoretical uncertainty in surface reflectivity (ρ) is $0.005 + 0.05\rho$ [Vermote and Kotchenova, 2008]), the error from the BRDF data in our ACAM NO₂ VCDs is estimated to be 4%.

The error in ACAM retrievals could also arise from insufficient knowledge of aerosol optical depth, the relative vertical distribution of aerosol and NO₂, and aerosol type [Martin et al., 2002; Leitão et al., 2010; Lin et al., 2014]. To derive aerosol-driven uncertainty in ACAM NO₂ retrievals, we conducted multiple sensitivity simulations by modulating the AOD and vertical distribution of aerosols. Assuming a typical uncertainty of 20% in MODIS AOD data used to constrain model aerosol profiles, the AOD contribution to the estimated uncertainty in NO₂ VCD is rather small at 2%. Our retrieval simulations were also performed with a gradual descent of the peak altitude of aerosol extinction, which may arise from hourly or daily PBL development, suggesting that

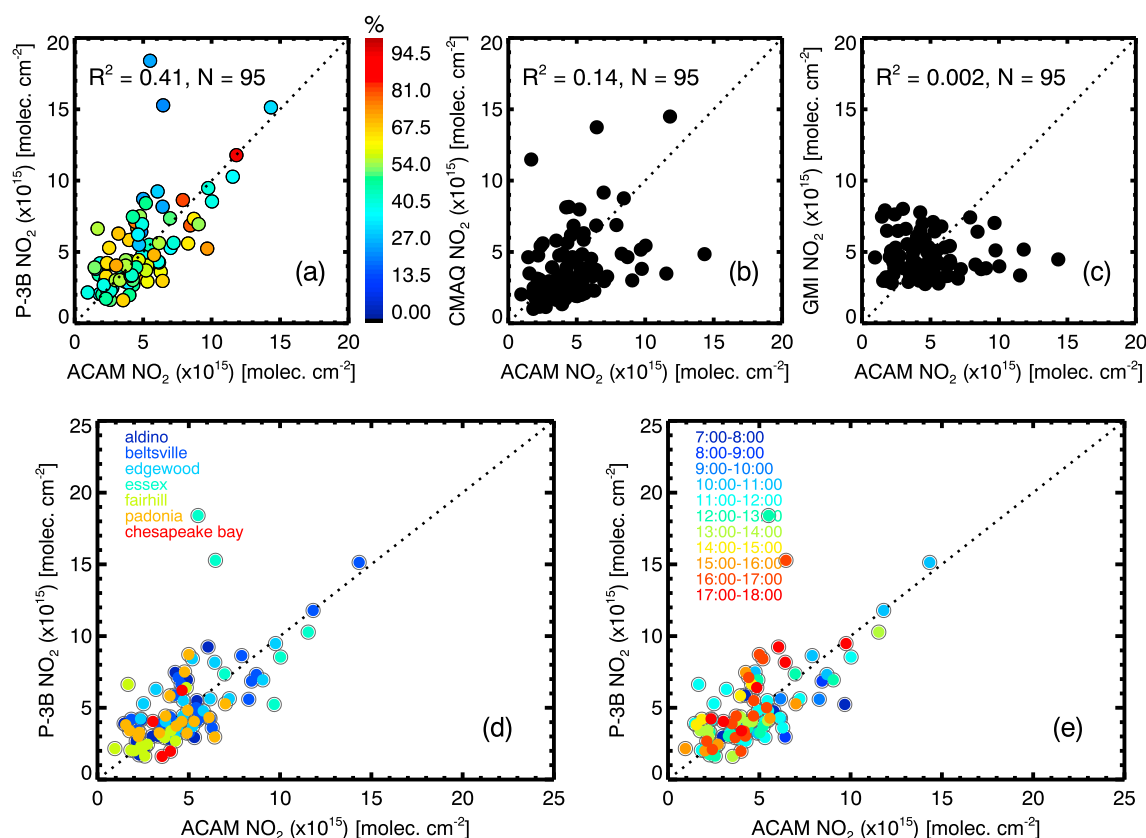


Figure 8. (top) NO_2 columns from ACAM are compared with those from (a) P-3B measurements and (b) CMAQ and (c) GMI simulations. P-3B data are color-coded by the percentage of extrapolated portions relative to total columns below ACAM altitudes. (bottom) Comparison of NO_2 columns from ACAM and P-3B color-coded by (d) location and (e) time range. The dotted line represents the 1:1 relationship.

the uncertainty in the vertical distribution of aerosols contributes considerable ($\sim 21\%$) uncertainty in the ACAM NO_2 retrievals.

3.5. Comparisons with other Data Sets

In this section, we compare the ACAM NO_2 retrievals with independent measurements from P-3B aircraft spirals, ground-based Pandora spectrometers, and from the OMI. These instruments deliver column abundances over different portions of the atmosphere. For example, Pandora gives total column NO_2 abundances, whereas aircraft measurements provide only a large part of tropospheric column. To address sampling differences in the vertical, we use coincidentally sampled model profiles to account for the missing (unmeasured) portions of the atmosphere. The collocation criterion for the differences in measurement time is < 10 min. For P-3B, the collocation criterion is 10 min from the sampling (spiral) window of ~ 20 min.

Figure 8 shows ACAM NO_2 columns and vertically integrated in situ aircraft measurements for all flight days in July 2011. The P-3B aircraft spirals covered different altitude ranges, varying with location, from ~ 300 m in the boundary layer to ~ 5 km in the free troposphere. Profiles taken over the Beltsville site were limited to a maximum altitude of 2.03 km due to local air traffic restrictions. To compare the two aircraft measurements in a meaningful way, it is necessary to assume a complete NO_2 profile below the ACAM altitude. We achieved this by combining the P-3B measured values with a GMI profile above the highest aircraft level and a CMAQ profile below the lowest aircraft level. This potentially impairs the comparison, since the P-3B measurements on average represent 51.8% of the columns measured by ACAM. Model-based extrapolations of the P-3B profiles below and above the aircraft on average are respectively 36.1% and 12.0% of the column below the ACAM altitude, although extrapolation at times could dominate the measurement portion. Despite this, data from the two measurements correlate ($R^2 = 0.41$, $N = 95$) and agree well (mean difference = 5%). Tables 1 and 2

Table 1. Summary of Comparisons Between ACAM With P-3B and Pandora Measurements at Various DISCOVER-AQ Sites

Sites	ACAM Versus P-3B			ACAM Versus Pandora		
	ACAM/P-3B	R^2 ^a	Sample Size	ACAM/Pandora	R^2	Sample Size
Aldino	0.87	0.41	14	0.93	0.08	73
Beltsville	1.03	0.73	21	1.09	0.30	79
Edgewood	0.96	0.40	19	1.25	0.31	82
Essex	0.77		6	1.78	0.54	47
Fairhill	0.93	0.11	14	2.22	0.20	138
Padonia	0.96	0.10	17	1.72	0.16	84
GSFC ^b				1.06	0.63	50
SERC ^c				1.13	0.39	65
UMBC ^d				0.97	0.85	87
UMCP ^e				1.20	0.50	24
Chesapeake Bay	1.09		4			

^aCorrelation coefficients (R) are not reported if sample size <8.

^bGoddard Space Flight Center, Greenbelt, MD.

^cSmithsonian Environmental Research Center, Edgewater, MD.

^dUniversity of Maryland, Baltimore County, Baltimore, MD.

^eUniversity of Maryland, College Park, MD.

contain summaries of these comparisons, segregated by location and time. Although ACAM and P-3B NO₂ column measurements are highly correlated in some instances ($R^2 > 0.8$), correlations for individual location and hour vary considerably and range from poor to good ($R^2 = 0.1$ – 0.8). Correlations tend to increase with increasing pollution levels. Correlations are usually low at clean sites where natural variability is small and NO₂ amounts are close to the detection limits of the two measurements. In some instances, a linear fit gives higher correlation when signals are higher, even when the measurements do not agree. Here we have not made any attempts to apply weights to the individual data points to account for the higher uncertainty associated with data having lower signal. The largest differences are observed over Chesapeake Bay (ACAM > P-3B) and Essex (ACAM < P-3B), where comparisons are complicated by larger retrieval or model errors and the complex vertical and horizontal distributions of NO₂, typical of areas affected by a bay breeze.

Figure 8 also shows comparisons between measured and model NO₂ columns over the DISCOVER-AQ domain. The CMAQ-simulated NO₂ columns are lower than ACAM and P-3B measurements by 18.8% and 23.3%, respectively, but they exhibit a poor correlation ($R^2 = 0.14$ for ACAM and $R^2 = 0.15$ for P-3B). In contrast, the GMI simulations agree better with the measurements (mean difference < 10%), albeit with no correlation.

Figure 9 and Tables 1 and 2 present comparisons of coincident NO₂ column retrievals from the ACAM and Pandora instruments. Although Pandora direct-Sun measurements allow retrievals of total and stratospheric NO₂ column retrievals [Herman *et al.*, 2009], the latter are not currently available. We subtract

Table 2. Summary of Comparisons Between ACAM With P-3B and Pandora Measurements Over Time of the Day

Local Time	ACAM Versus P-3B			ACAM Versus Pandora		
	ACAM/P-3B	R^2	Sample Size	ACAM/Pandora	R^2	Sample Size
7:00–8:00	1.20		4	1.14	0.38	18
8:00–9:00	1.45		5	1.62	0.77	30
9:00–10:00	1.28		2	1.47	0.73	29
10:00–11:00	1.02	0.86	8	1.26	0.78	84
11:00–12:00	1.00	0.20	19	1.26	0.65	126
12:00–13:00	0.90	0.27	15	1.14	0.60	119
13:00–14:00	1.04	0.82	11	1.14	0.34	57
14:00–15:00	0.60		4	0.73	0.52	38
15:00–16:00	0.95		6	1.10	0.43	82
16:00–17:00	0.81	0.62	15	1.43	0.31	96
17:00–18:00	0.81		7	1.35	0.53	52

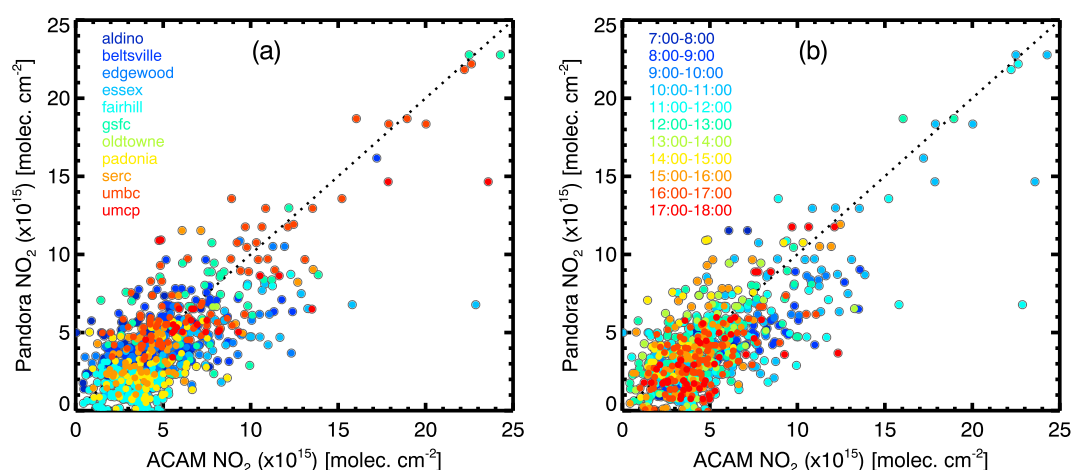


Figure 9. Comparison between ACAM and Pandora NO_2 VCDs separated by color-coded (a) observational sites and (b) measurement times. Modeled stratospheric NO_2 values are subtracted from Pandora data for a direct comparison. The dotted line represents the 1:1 relationship.

estimates of the NO_2 column above the aircraft from coincidentally sampled GMI simulations, scaling the stratospheric portion diurnally with results from coincident stratospheric NO_2 column data from OMI and GMI, to derive Pandora NO_2 columns below the aircraft. This reliance on model output likely affects the comparison over less polluted areas of the DISCOVER-AQ domain. Nevertheless, NO_2 retrievals from ACAM and Pandora are highly consistent. Measurements from the two instruments exhibit a significant correlation ($R^2 = 0.60$, $N = 731$), with the largest correlation ($R^2 = 0.73\text{--}0.85$) in the late morning and over polluted sites. While ACAM and Pandora measurements generally agree to within 26%, the mean relative difference between them is 23.1%. Large discrepancies in the morning and late afternoon hours, when observations are made at large solar angles, are likely due to the sampling of different air masses by the two instruments. Inconsistent results at Fairhill and Padonia, with excellent agreement between ACAM and P-3B and nearly a factor of two differences with Pandora, may reflect a combination of enhanced spatial variation and placement of the Pandora instruments.

Figure 10 compares the NO_2 columns retrieved from the ACAM and OMI. The tropospheric portion above the aircraft was calculated from coincidentally sampled GMI NO_2 profiles and subtracted from the OMI tropospheric NO_2 data. Figure 10a shows an example of coincident NO_2 observations made by the two instruments on 29 July 2011. This clearly demonstrates unprecedented new insights into spatial variation and complexities behind NO_2 validation. Overall, both ACAM and OMI observations are similar in their spatial patterns, with large columns over major urban centers that reflect industrialization and dense traffic. However, the OMI ground pixel areas are quite large, with a much smoother field of NO_2 ; in reality the NO_2 field exhibits intraurban spatial variability as captured by ACAM. An enlarged view of one of the OMI ground pixels with an area of about 1050 km^2 (at the cross-track position of 8) shown in Figure 10d provides quantitative evidence of a factor of 4 subpixel variability, yet at the same time, retrievals from the two independent measurements agree within the range of their uncertainties (average difference = 19.5%).

Figure 10b displays OMI NO_2 columns compared with spatially averaged ACAM retrievals for OMI footprints. Data from the two instruments are well correlated ($R^2 = 0.61$, $N = 20$). The NO_2 columns from ACAM are on average 10.3% higher than those for OMI, but the data for individual OMI pixels differ by up to 32%. The agreement improves with the increase in the number of ACAM samples, suggesting that the spatial averaging of ACAM observations over OMI pixels at times could cover only a fraction of the pixel area, and therefore, the validation exercise could still be compromised by the representativeness issue.

Figure 10c shows collocated observations from ACAM and OMI for all flight days in July 2011. In this case, the average difference is somewhat larger (16%) and the correlation is moderate ($R^2 = 0.34$, $N = 104$). Occasional large discrepancies of up to a factor of 2 are evident. Such results ought to be expected due to differences in the sampling area and potential NO_2 spatial inhomogeneity within a satellite ground pixel.

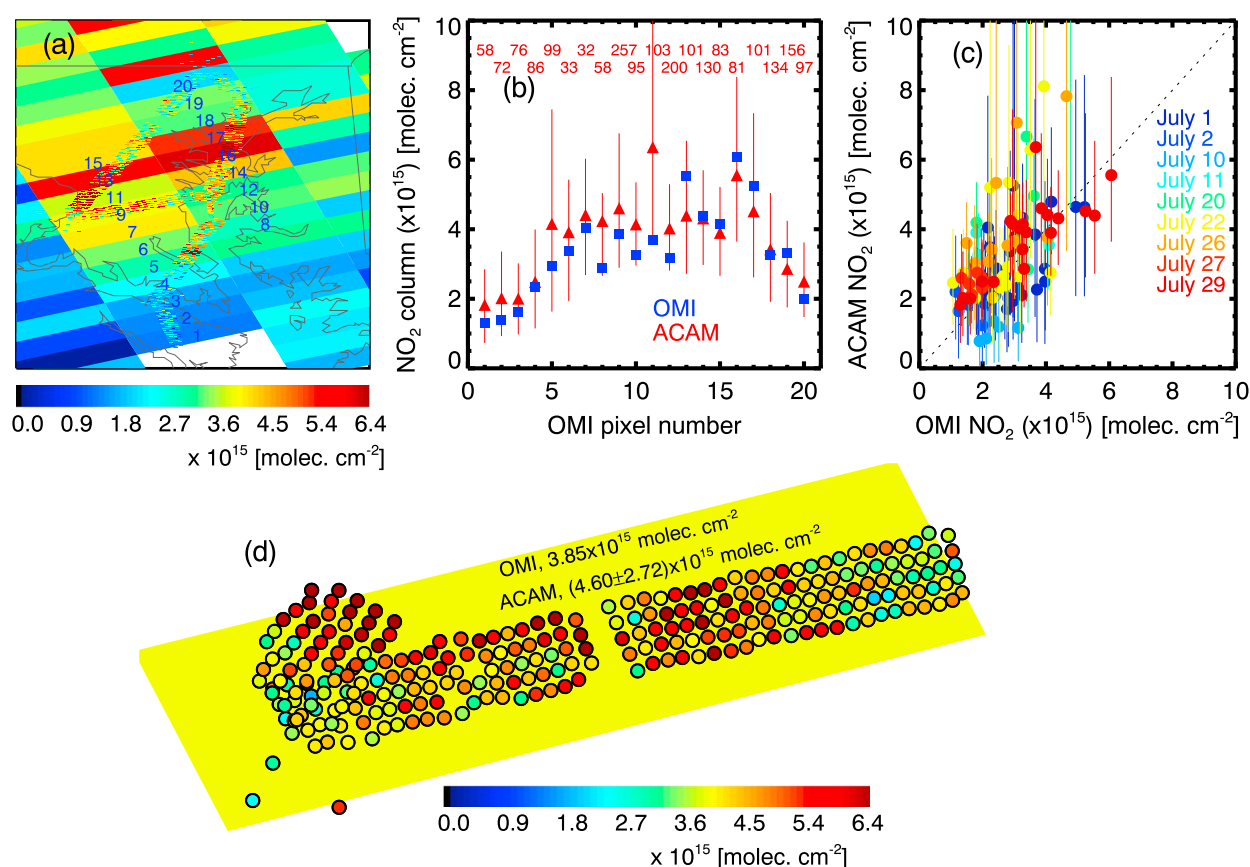


Figure 10. Comparisons between ACAM and OMI NO₂. (a) Coincidentally sampled (± 30 min of OMI measurements) ACAM NO₂ observations are overlaid on the OMI NO₂ map for 29 July 2011. (b) Collocated OMI pixels are numbered to compare the OMI (blue) and pixel-averaged ACAM data (red). The number of ACAM measurements within each OMI pixel is shown in red color in the legend. The vertical bars represent the standard deviations of the ACAM data. (c) A summary plot showing comparison of OMI and pixel-wise average ACAM data during the DISCOVER-AQ field campaign. The dotted line represents the 1:1 relationship. (d) The ninth OMI pixel from the cross-track position of 8 is enlarged to illustrate NO₂ spatial variability observed by ACAM on the OMI pixel. ACAM data are presented in circles.

4. Conclusions

We presented the first detailed retrieval studies of tropospheric NO₂ from the Airborne Compact Atmospheric Mapper (ACAM)—an instrument that was designed to provide cost-effective airborne remote sensing observations of tropospheric pollutants. ACAM has participated in about a half-dozen field campaigns, including the NASA Earth Venture program DISCOVER-AQ missions. ACAM was a part of the first DISCOVER-AQ field campaign held in the Baltimore-Washington DC region in July 2011, and it has provided unprecedented new insights through high-resolution spatial and temporal mapping of NO₂ from the NASA UC-12 platform.

Our retrieval approach for ACAM is similar to that for satellite NO₂ retrievals, consisting of retrieval of differential NO₂ slant columns from measurements of backscattered solar radiation between 425 and 460 nm by using the differential optical absorption spectroscopy (DOAS) method, calculation of air mass factors (AMFs) by using a radiative transfer model, and calculation of NO₂ vertical columns below the aircraft. The AMFs were calculated with the vector linearized discrete ordinate radiative transfer (VLIDORT) code, based on ACAM's measurement conditions, with surface inputs based on MODIS-derived high-resolution bidirectional reflectance distribution functions (BRDFs) to account for surface reflectance anisotropy, the vertical distribution of aerosols to account for aerosol optical effects, and diurnally varying NO₂ profiles from the Community Multiscale Air Quality (CAMQ) and Global Modeling Initiative (GMI) models. Our assessment of simulated planetary boundary layer (PBL) and NO₂ profiles with surface- and aircraft-based in situ measurements indicated that CMAQ captures the diurnal variation in NO₂ mixing, vertical distribution, and column

amount in the PBL reasonably well, although it generally underestimates the free-tropospheric NO₂. The GMI simulated free-tropospheric and stratospheric NO₂ data are consistent with observations. We conducted a series of analyses to understand how various parameters affect the vertical sensitivity of the ACAM measurements below and above the aircraft.

We compared ACAM NO₂ retrievals with NO₂ column observations from ground-based Pandora and satellite-based Ozone Monitoring Instrument (OMI) as well as in situ NO₂ measurements from the NASA P-3B aircraft. Data from coincident ACAM and P-3B measurements agree well, with a coefficient of determination (R^2) of 0.41 and an average difference of 5%. Segregation of results by location and time suggests differences generally <13% and somewhat larger differences over Chesapeake Bay and Essex, where bay breezes could influence the NO₂ fields, and in the morning hours, when mixing layer depth changes rapidly. Comparisons with Pandora retrievals also show good agreement, with $R^2=0.60$ and mean difference = 23.1%. Large discrepancies are observed in the morning and late afternoon hours, potentially due to differences in sampling direction. Comparison with the OMI measurements suggests that there could be considerable subpixel variability within OMI pixels, but OMI and spatially averaged ACAM data agree reasonably well. Differences between observations vary by day, reaching 10.3% ($R^2 = 0.61$) on July 29 and 16% ($R^2 = 0.34$) for the month of July.

Acknowledgments

We thank two anonymous reviewers for helpful comments that improved the manuscript. We would like to thank Andrew J. Weinheimer from the National Center for Atmospheric Research for making the P-3B data available. The data generated from this study will be made available from NASA's DISCOVER-AQ archive (<http://www-air.larc.nasa.gov/missions/discover-aq/dataaccess.htm>). The model data and routines used to make figures will be made available from the authors upon request. The work was supported by NASA's Earth Venture DISCOVER-AQ project.

References

- Anand, J. S., P. S. Monks, and R. J. Leigh (2015), An improved retrieval of tropospheric NO₂ from space over polluted regions using an Earth radiance reference, *Atmos. Meas. Tech.*, **8**, 1519–1535, doi:10.5194/amt-8-1519-2015.
- Anderson, D. C., C. P. Loughner, A. Weinheimer, T. P. Canty, R. J. Salawitch, H. Worden, A. Fried, T. Mikoviny, A. Wisthaler, and R. R. Dickerson (2014), Measured and modeled CO and NO_y in DISCOVER-AQ: An evaluation of emissions and chemistry over the eastern US, *Atmos. Environ.*, **96**, 78–87.
- Baidar, S., H. Oetjen, S. Coburn, B. Dix, I. Ortega, R. Sinreich, and R. Volkamer (2013), The CU Airborne MAX-DOAS instrument: Vertical profiling of aerosol extinction and trace gases, *Atmos. Meas. Tech.*, **6**, 719–739, doi:10.5194/amt-6-719-2013.
- Bass, A. M. and R. J. Paur (1985), The ultraviolet cross-sections of ozone. I. The measurements, II – Results and temperature dependence, in *Atmospheric ozone. Proceedings of the Quadrennial Ozone Symposium*, pp. 606–616, D. Reidel, Dordrecht Netherlands.
- Bey, I., D. J. Jacob, R. M. Yantosca, J. A. Logan, B. D. Field, A. M. Fiore, Q. Li, H. Y. Liu, L. J. Mickley, and M. G. Schultz (2001), Global modeling of tropospheric chemistry with assimilated meteorology: Model description and evaluation, *J. Geophys. Res.*, **106**, 23,073–23,095, doi:10.1029/2001JD000807.
- Boersma, K. F., D. J. Jacob, H. J. Eskes, R. W. Pinder, J. Wang, and R. J. van der A (2009), Intercomparison of SCIAMACHY and OMI tropospheric NO₂ columns: Observing the diurnal evolution of chemistry and emissions from space, *J. Geophys. Res.*, **113**, D16S26, doi:10.1029/2007JD008816.
- Bracher, A., M. Sinnhuber, A. Rozanov, and J. P. Burrows (2005), Using a photochemical model for the validation of NO₂ satellite measurements at different solar zenith angles, *Atmos. Chem. Phys.*, **5**, 393–408, doi:10.5194/acp-5-393-2005.
- Brewer, A. C., C. T. McElroy, and J. B. Kerr (1973), Nitrogen dioxide concentrations in the atmosphere, *Nature*, **246**, 129–133.
- Bucselu, E. J., N. A. Krotkov, E. A. Celarier, L. N. Lamsal, W. H. Swartz, P. K. Bhartia, K. F. Boersma, J. P. Veefkind, J. F. Gleason, and K. E. Pickering (2013), A new stratospheric and tropospheric NO₂ retrieval algorithm for nadir-viewing satellite instruments: Applications to OMI, *Atmos. Meas. Tech.*, **6**, 2607–2626, doi:10.5194/amt-6-2607-2013.
- Burnett, R. T., D. Steib, J. R. Brook, S. Cakmak, R. Dales, M. Raizenne, R. Vincent, and T. Dann (2004), The short-term effects of nitrogen dioxide on mortality in Canadian cities, *Arch. Environ. Health*, **59**(404), 228–237.
- Burrows, J. P., et al. (1999), The Global Ozone Monitoring Experiment (GOME): Mission concept and first scientific results, *J. Atmos. Sci.*, **56**, 151–175.
- Byun, D., and K. L. Schere (2006), Review of the governing equations, computational algorithms, and other components of the Models-3 Community Multiscale Air Quality (CMAQ) modeling system, *Appl. Mech. Rev.*, **59**, 51–77.
- Callies, J., E. Corpaccioli, M. Eisinger, A. Hahne, and A. Lefebvre (2000), GOME-2—MetOp's second-generation sensor for operational ozone monitoring, *ESA Bull.*, **102**, 28–36.
- Chance, K. V., and R. D. J. Spurr (1997), Ring effect studies: Rayleigh scattering, including molecular parameters for rotational Raman scattering, and the Fraunhofer spectrum, *Appl. Opt.*, **36**, 21.
- Chance, K., X. Liu, R. M. Suleiman, D. E. Flittner, J. Al-Saadi, and S. J. Janz (2013), Tropospheric emissions: Monitoring of pollution (TEMPO), SPIE Publication 8866-11.
- Day, D. A., P. J. Wooldridge, M. B. Dillon, J. A. Thornton, and R. C. Cohen (2002), A thermal dissociation laser-induced fluorescence instrument for in situ detection of NO₂, peroxy nitrates, alkyl nitrates, and HNO₃, *J. Geophys. Res.*, **107**(D6), 4046, doi:10.1029/2001JD000779.
- Dobber, M., Q. Kleipool, R. Dirksen, P. Levelt, G. Jaross, S. Taylor, T. Kelly, L. Flynn, G. Leppelmeier, and N. Rozemeijer (2008), Validation of Ozone Monitoring Instrument level 1b data products, *J. Geophys. Res.*, **113**, D15S06, doi:10.1029/2007JD008665.
- Douglass, A. R., R. S. Stolarski, S. E. Strahan, and P. S. Connell (2004), Radicals and reservoirs in the GMI chemistry and transport model: Comparison to measurements, *J. Geophys. Res.*, **109**, D16302, doi:10.1029/2004JD004632.
- Drury, E., D. J. Jacob, R. J. D. Spurr, J. Wang, Y. Shinozuka, B. E. Anderson, A. D. Clarke, J. Dibb, C. McNaughton, and R. Weber (2010), Synthesis of satellite (MODIS), aircraft (ICARTT), and surface (IMPROVE, EPA-AQS, AERONET) aerosol observations over eastern North America to improve MODIS aerosol retrievals and constrain surface aerosol concentrations and sources, *J. Geophys. Res.*, **115**, D14204, doi:10.1029/2009JD012629.
- Fairlie, T. D., D. J. Jacob, J. E. Dibb, B. Alexander, M. A. Avery, A. van Donkelaar, and L. Zhang (2010), Impact of mineral dust on nitrate, sulfate, and ozone in transpacific Asian pollution plumes, *Atmos. Chem. Phys.*, **10**, 3999–4012, doi:10.5194/acp-10-3999-2010.

- Flynn, C. M., K. E. Pickering, J. H. Crawford, A. J. Weinheimer, G. Diskin, K. L. Thornhill, C. Loughner, P. Lee, and S. A. Strode (2016), Variability of O_3 and NO_2 profile shapes during DISCOVER-AQ: Implications for satellite observations and comparisons to model-simulated profiles, *Atmos. Environ.*, **147**, 133–156.
- Fountoukis, C., and A. Nenes (2007), ISORROPIA II: A computationally efficient thermodynamic equilibrium model for K^+ – Ca^{2+} – Mg^{2+} – NH_4^+ – Na^+ – SO_4^{2-} – NO_3^- – Cl^- – H_2O aerosols, *Atmos. Chem. Phys.*, **7**, 4639–4659, doi:10.5194/acp-7-4639-2007.
- Greenblatt, G. D., J. J. Orlando, J. B. Burkholder, and A. R. Ravishankara (1990), Absorption measurements of oxygen between 330 and 140 nm, *J. Geophys. Res.*, **95**, 18,577–18,582, doi:10.1029/JD095iD11p18577.
- Hains, J. C., et al. (2010), Testing and improving OMI DOMINO tropospheric NO_2 using observations from the DANDELIONS and INTEX-B validation campaigns, *J. Geophys. Res.*, **115**, D05301, doi:10.1029/2009JD012399.
- Heckel, A., S.-W. Kim, G. J. Frost, A. Richter, M. Trainer, and J. P. Burrows (2011), Influence of low spatial resolution a priori data on tropospheric NO_2 satellite retrievals, *Atmos. Meas. Tech.*, **4**, 1805–1820, doi:10.5194/amt-4-1805-2011.
- Herman, J., A. Cede, E. Spinei, G. Mount, M. Tzortziou, and N. Abuhassan (2009), NO_2 column amounts from ground-based Pandora and MFDOAS spectrometers using the direct-Sun DOAS technique: Intercomparisons and application to OMI validation, *J. Geophys. Res.*, **114**, D13307, doi:10.1029/2009JD011848.
- Hong, S. Y., and J.-O. J. Lim (2006), The WRF Single-Moment 6-Class Microphysics Scheme (WSM6), *J. Korean Meteor. Soc.*, **42**, 129–151.
- Jaeglé, L., P. K. Quinn, T. S. Bates, B. Alexander, and J.-T. Lin (2011), Global distribution of sea salt aerosols: New constraints from in situ and remote sensing observations, *Atmos. Chem. Phys.*, **11**, 3137–3157, doi:10.5194/acp-11-3137-2011.
- Juseon, B., J. H. Kim, X. Liu, K. Chance, and J. Kim (2013), Evaluation of ozone profile and tropospheric ozone retrievals from GEMS and OMI spectra, *Atmos. Meas. Tech.*, **6**, 239–249, doi:10.5194/amt-6-239-2013.
- Kowalewski, M. G., and S. J. Janz (2009), Remote sensing capabilities of the Airborne Compact Atmospheric Mapper, *Proc. SPIE*, **7452**, doi:10.1117/12.827035.
- Lamsal, L. N., R. V. Martin, M. Steinbacher, E. A. Celarier, E. Bucsela, E. J. Dunlea, and J. Pinto (2008), Ground level nitrogen dioxide concentrations inferred from the satellite-borne Ozone Monitoring Instrument, *J. Geophys. Res.*, **113**, D16308, doi:10.1029/2007JD009235.
- Lamsal, L. N., et al. (2014), Evaluation of OMI operational standard NO_2 column retrievals using in situ and surface-based NO_2 observations, *Atmos. Chem. Phys.*, **14**, 11,587–11,609, doi:10.5194/acp-14-11587-2014.
- Lamsal, L. N., B. N. Duncan, Y. Yoshida, N. A. Krotkov, K. E. Pickering, D. G. Streets, and Z. Lu (2015), U.S. NO_2 trends (2005–2013): EPA Air Quality System (AQS) data versus improved observations from the Ozone Monitoring Instrument (OMI), *Atmos. Environ.*, **110**, 130–143, doi:10.1016/j.atmosenv.2015.03.055.
- Laughner, J. L., A. Zare, and R. C. Cohen (2016), Effects of daily meteorology on the interpretation of space-based remote sensing of NO_2 , *Atmos. Chem. Phys. Discuss.*, doi:10.5194/acp-2016-536.
- Leitão, J., A. Richter, M. Vrekoussis, A. Kokhanovsky, Q. J. Zhang, M. Beekmann, and J. P. Burrows (2010), On the improvement of NO_2 satellite retrievals—Aerosol impact on the air mass factors, *Atmos. Meas. Tech.*, **3**, 475–493, doi:10.5194/amt-3-475-2010.
- Levelt, P. F., G. H. J. van den Oord, M. R. Dobber, A. Malkki, H. Visser, J. de Vries, P. Stammes, J. Lundell, and H. Saari (2006), The Ozone Monitoring Instrument, *IEEE Trans. Geotherm. Remote Sens.*, **44**(5), 1093–1101, doi:10.1109/TGRS.2006.872333.
- Lin, J.-T., R. V. Martin, K. F. Boersma, M. Sneep, P. Stammes, R. Spurr, P. Wang, M. Van Roozendaal, K. Clémer, and H. Irie (2014), Retrieving tropospheric nitrogen dioxide from the Ozone Monitoring Instrument: Effects of aerosols, surface reflectance anisotropy, and vertical profile of nitrogen dioxide, *Atmos. Chem. Phys.*, **14**, 1441–1461, doi:10.5194/acp-14-1441-2014.
- Liu, C., X. Liu, M. G. Kowalewski, S. J. Janz, G. González Abad, K. E. Pickering, K. Chance, and L. N. Lamsal (2015), Analysis of ACAM data for trace gas retrievals during the 2011 DISCOVER-AQ campaign, *J. Spectroscopy*, **2015**, 827160.
- Loughner, C. P., D. J. Allen, K. E. Pickering, D.-L. Zhang, Y.-X. Shou, and R. R. Dickerson (2011), Impact of fair-weather cumulus clouds and the Chesapeake Bay breeze on pollutant transport and transformation, *Atmos. Environ.*, **45**, 4060–4072.
- Loughner, C. P., et al. (2014), Impact of bay breeze circulations on surface air quality and boundary layer export, *J. Appl. Meteorol. Climatol.*, **53**, 1697–1713.
- Marchenko, S., N. A. Krotkov, L. N. Lamsal, E. A. Celarier, W. H. Swartz, and E. J. Bucsela (2015), Revising the slant-column density retrieval of nitrogen dioxide observed by the Ozone Monitoring Instrument, *J. Geophys. Res. Atmos.*, **120**, 5670–5692, doi:10.1002/2014JD022913.
- Martin, R. V., et al. (2002), Unimproved retrieval of tropospheric nitrogen dioxide from GOME, *J. Geophys. Res.*, **107**(D20), 4437, doi:10.1029/2001JD001027.
- Merlaud, A., M. Van Roozendaal, J. van Gent, C. Fayt, J. Maes, X. Toledo-Fuentes, O. Ronveaux, and M. De Mazière (2012), DOAS measurements of NO_2 from an ultralight aircraft during the Earth Challenge expedition, *Atmos. Meas. Tech.*, **5**, 2057–2068, doi:10.5194/amt-5-2057-2012.
- Nowlan, C. R., et al. (2016), Nitrogen dioxide observations from the Geostationary Trace gas and Aerosol Sensor Optimization (GeoTASO) airborne instrument: Retrieval algorithm and measurements during DISCOVER-AQ Texas 2013, *Atmos. Meas. Tech.*, **9**, 2647–2668, doi:10.5194/amt-9-2647-2016.
- Oetjen, H., S. Baidar, N. A. Krotkov, L. N. Lamsal, M. Lechner, and R. Volkamer (2013), Airborne MAX-DOAS measurements over California: Testing the NASA OMI tropospheric NO_2 product, *J. Geophys. Res. Atmos.*, **118**, 7400–7413, doi:10.1002/jgrd.50550.
- Palmer, P. I., D. J. Jacob, K. Chance, R. V. Martin, R. J. D. Spurr, T. P. Kuros, I. Bey, R. Yantosca, A. Fiore, and Q. Li (2001), Air mass factor formulation for spectroscopic measurements from satellites: Application to formaldehyde retrievals from the Global Ozone Monitoring Experiment, *J. Geophys. Res.*, **106**, 14,539–14,550, doi:10.1029/2000JD900772.
- Park, R. J., D. J. Jacob, N. Kumar, and R. M. Yantosca (2006), Regional visibility statistics in the United States: Natural and transboundary pollution influences, and implications for the Regional Haze Rule, *Atmos. Environ.*, **40**, 5405–5423, doi:10.1016/j.atmosenv.2006.04.059.
- Platt, U., and J. Stutz (2006), *Differential Optical Absorption Spectroscopy (DOAS), principle and applications*, Springer, Heidelberg, isbn:3-340-21193-4.
- Pleim, J. E., and J. Chang (1992), A non-local closure model for vertical mixing in the convective boundary layer, *Atmos. Environ.*, **26A**, 965–981.
- Pleim, J. E., A. Xiu, P. L. Finkelstein, and T. L. Otte (2001), A coupled land-surface and dry deposition model and comparison to field measurements of surface heat, moisture, and ozone fluxes, *Water Air Soil Pollut. Focus*, **1**, 243–252.
- Popp, C., D. Brunner, A. Damm, M. Van Roozendaal, C. Fayt, and B. Buchmann (2012), High-resolution NO_2 remote sensing from the Airborne Prism Experiment (APEX) imaging spectrometer, *Atmos. Meas. Tech.*, **5**, 2211–2225, doi:10.5194/amt-5-2211-2012.
- Poulida, O., K. L. Civerolo, and R. R. Dickerson (1994), Observations and tropospheric photochemistry in central North Carolina, *J. Geophys. Res.*, **99**, 10,553–10,563, doi:10.1029/94JD00404.
- Ridley, B. A., and F. E. Grahek (1990), A small, low flow, high-sensitivity reaction vessel for NO chemiluminescence detectors, *J. Atmos. Oceanic Technol.*, **7**, 307–311.
- Ridley, B., et al. (2004), Florida thunderstorms: A faucet of reactive nitrogen to the upper troposphere, *J. Geophys. Res.*, **109**, D17305, doi:10.1029/2004JD004769.

- Rienecker, M. M., et al. (2008), The GEOS-5 data assimilation system—Documentation of versions 5.0.1, 5.1.0, and 5.2.0, NASA Tech. Memo., NASA/TM-2008-104606, vol. 27, 118 pp.
- Rothman, L., et al. (2005), The HITRAN 2004 molecular spectroscopic database, *J. Quant. Spectrosc. Radiat. Transfer*, *96*, 139–204, doi:10.1016/j.jqsrt.2004.10.008.
- Russell, A. R., A. E. Perring, L. C. Valin, E. J. Bucsela, E. C. Browne, P. J. Wooldridge, and R. C. Cohen (2011), A high spatial resolution retrieval of NO₂ column densities from OMI: Method and evaluation, *Atmos. Chem. Phys.*, *11*, 8543–8554, doi:10.5194/acp-11-8543-2011.
- Samoli, E., et al. (2006), Short term effects of nitrogen dioxide and mortality: An analysis within the APHEA project, *Eur. Respir. J.*, *27*, 1129–1137.
- Schaaf, C. L. B., J. Liu, F. Gao, and A. H. Strahler (2011), MODIS albedo and reflectance anisotropy products from Aqua and Terra, in *Land Remote Sensing and Global Environmental Change: NASA's Earth Observing System and the Science of ASTER and MODIS, Remote Sens. and Digital Image Process. Ser.*, vol. 11, edited by B. Ramachandran, C. Justice, and M. Abrams, pp. 873, Springer-Verlag, New York.
- Shindell, D. T., G. Faluvegi, D. M. Koch, G. A. Schmidt, N. Unger, and S. E. Bauer (2009), Improved attribution of climate forcing to emissions, *Science*, *326*, 716–718, doi:10.1126/science.1174760.
- Skamarock, W. C., J. B. Klemp, J. Dudhia, D. O. Gill, D. L. Barker, M. G. Duda, X.-Y. Huang, W. Wang, and J. G. Powers (2008), A description of the Advanced Research WRF version 3, NCAR Technical Note, NCAR/TN-475+STR, NCAR, Boulder, Colo.
- Spinei, E., A. Cede, W. H. Swartz, J. Herman, and G. H. Mount (2014), The use of NO₂ absorption cross section temperature sensitivity to derive NO₂ profile temperature and stratospheric-tropospheric column partitioning from visible direct-Sun DOAS measurements, *Atmos. Meas. Tech.*, *7*, 4299–4316, doi:10.5194/amt-7-4299-2014.
- Spurr, R. (2008), in *LIDORT and VLIDORT: Linearized Pseudo-Spherical Scalar and Vector Discrete Ordinate Radiative Transfer Models for Use in Remote Sensing Retrieval Problems, Light Scattering Rev.*, vol. 3, edited by A. Kokhanovsky, Springer-Verlag, Berlin.
- Spurr, R., J. Wang, J. Zeng, and M. I. Mishchenko (2012), Linearized T-matrix and Mie scattering computations, *J. Quant. Spectrosc. Radiat. Transfer*, *113*, 425–439.
- Strahan, S. E., B. N. Duncan, and P. Hoor (2007), Observationally derived transport diagnostics for the lowermost stratosphere and their application to the GMI chemistry and transport model, *Atmos. Chem. Phys.*, *7*, 2435–2445, doi:10.5194/acp-7-2435-2007.
- Strode, S. A., J. M. Rodriguez, J. A. Logan, O. R. Cooper, J. C. Witte, L. N. Lamsal, M. Damon, B. Van Aartsen, S. D. Steenrod, and S. E. Strahan (2015), Trends and variability in surface ozone over the United States, *J. Geophys. Res. Atmos.*, *120*, 9020–9042, doi:10.1002/2014JD022784.
- Tewari, M., F. Chen, W. Wang, J. Dudhia, M. A. LeMone, K. Mitchell, M. Ek, G. Gayno, and J. Wegiel, and R. H. Cuenca, 2004, Implementation and verification of the unified NOAA land surface model in the WRF model, paper presented at 20th Conference on Weather Analysis and Forecasting/16th Conference on Numerical Weather Prediction, pp. 11–15.
- Thornton, J. A., P. J. Wooldridge, and R. C. Cohen (2000), Atmospheric NO₂: In situ laser-induced fluorescence detection at parts per trillion mixing ratios, *Anal. Chem.*, *72*, 528.
- United States Environmental Protection Agency (U.S. EPA) (2008), Integrated science assessment for oxides of nitrogen: Health criteria, Technical Report; U.S. EPA: Research Triangle Park, NC, EPA/600/R-07/093.
- Valin, L., A. Russell, R. Hudman, and R. Cohen (2011), Effects of model resolution on the interpretation of satellite NO₂ observations, *Atmos. Chem. Phys.*, *11*, 11647–11655, doi:10.5194/acp-11-11647-2011.
- van Donkelaar, A., R. V. Martin, M. Brauer and B. L. Boys (2014), Global fine particulate matter concentrations from satellite for long-term exposure assessment, *Environ. Health Perspect.*, doi:10.1289/ehp.1408646.
- Vandaele, A., C. Hermans, P. Simon, M. Carleer, R. Colin, S. Fally, M. Mérianne, A. Jenouvrier, and B. Coquart (1998), Measurements of the NO₂ absorption cross-section from 42,000 cm⁻¹ to 10,000 cm⁻¹ (238–1000 nm) at 220 K and 294 K, *J. Quant. Spectrosc. Radiat. Transfer*, *59*, 171–184, doi:10.1016/S0022-4073(97)00168-4.
- Vasilkov, A., Qin, W., Krotkov, N., Lamsal, L., Spurr, R., Haffner, D., Joiner, J., Yang, E.-S., and Marchenko, S. (2016), Accounting for the effects of surface BRDF on satellite cloud and trace-gas retrievals: A new approach based on geometry-dependent Lambertian-equivalent reflectivity applied to OMI algorithms, *Atmos. Meas. Tech. Discuss.*, doi:10.5194/amt-2016-133.
- Vermote, E. F., and S. Kotchenova (2008), Atmospheric correction for the monitoring of land surfaces, *J. Geophys. Res.*, *113*, D23590, doi:10.1029/2007JD009662.
- Volkamer, R., P. Spietz, J. P. Burrows, and U. Platt (2005), High-resolution absorption cross-section of Glyoxal in the UV/vis and IR spectral ranges, *J. Photochem. Photobiol., A*, *172*, 35–46, doi:10.1016/j.jphotochem.2004.11.011.
- Walter, D., K.-P. Heue, A. Rauthe-Schoech, C. A. M. Brenninkmeijer, L. N. Lamsal, N. Krotkov, and U. Platt (2012), Flux calculation using CARIBIC DOAS aircraft measurements—SO₂ emissions of Norilsk, *J. Geophys. Res.*, *117*, D11305, doi:10.1029/2011JD017335.
- Wittrock, F., H. Oetjen, A. Richter, S. Fietkau, T. Medeke, A. Rozanov, and J. P. Burrows (2004), MAX-DOAS measurements of atmospheric trace gases in Ny-Ålesund—Radiative transfer studies and their application, *Atmos. Chem. Phys.*, *4*, 955–966, doi:10.5194/acp-4-955-2004.
- Yarwood, G., S. Rao, M. Yocke, and G. Z. Whitten (2005), *Updates to the Carbon Bond Mechanism: CB05. RT-0400675*, U.S. Environmental Prediction Agency, Washington, D. C.
- Zender, C. S., Bian, H. S., and Newman, D. (2003), Mineral Dust Entrainment and Deposition (DEAD) model: Description and 1990s dust climatology, *J. Geophys. Res.*, *108*(D14), 4416, doi:10.1029/2002JD002775.
- Zhang, D.-L., and R. A. Anthes (1982), A high resolution model of the planetary boundary layer-sensitivity tests and comparisons with SESAME-79 data, *J. Appl. Meteorol.*, *21*, 1594–1609.
- Zhou, Y., D. Brunner, R. J. D. Spurr, K. F. Boersma, M. Sneep, C. Popp, and B. Buchmann (2010), Accounting for surface reflectance anisotropy in satellite retrievals of tropospheric NO₂, *Atmos. Meas. Tech.*, *3*, 1185–1203, doi:10.5194/amt-3-1185-2010.